



HHS Public Access

Author manuscript

J Med Chem. Author manuscript; available in PMC 2017 December 17.

Published in final edited form as:

J Med Chem. 2016 June 09; 59(11): 5311–5323. doi:10.1021/acs.jmedchem.6b00038.

Near-Infrared Illumination of Native Tissues for Image-Guided Surgery

Eric A. Owens^{†,#}, Hoon Hyun^{‡,§,#}, Tyler L. Dost^{†,#}, Jeong Heon Lee[‡], GwangLi Park[‡], Dang Huan Pham[§], Min Ho Park^{||}, Hak Soo Choi^{*,‡}, and Maged Henary^{*,†}

[†]Center for Diagnostics and Therapeutics, Center for Biotechnology and Drug Design, Department of Chemistry, Georgia State University, Petit Science Center, 100 Piedmont Ave SE, Atlanta, Georgia 30303, United States

[‡]Gordon Center for Medical Imaging, Division of Nuclear Medicine and Molecular Imaging, Department of Radiology, Massachusetts General Hospital and Harvard Medical School, Boston, Massachusetts 02114, United States

[§]Department of Biomedical Sciences, Chonnam National University Medical School, Gwangju 501-746, South Korea

^{||}Department of Surgery, Chonnam National University Medical School, Gwangju 501-746, South Korea

Abstract

Our initial efforts to prepare tissue-specific near-infrared (NIR) fluorescent compounds generated successful correlation between physicochemical properties and global uptake in major organs after systemic circulation and biodistribution. Herein, we focus on the effects on biodistribution based on modulating electronic influencing moieties from donating to withdrawing moieties at both the heterocyclic site and through *meso*-substitution of pentamethine cyanine fluorophores. These selected modifications harnessed innate biodistribution pathways through the structure-inherent targeting, resulting in effective imaging of the adrenal glands, pituitary gland, lymph nodes, pancreas, and thyroid and salivary glands. These native-tissue contrast agents will arm surgeons with a powerful and versatile arsenal for intraoperative NIR imaging in real time.

Graphical Abstract

*Corresponding Authors: Phone: 404-413-5566. mhenary1@gsu.edu. Fax: 404-413-5505. Phone: 617-726-5784. hchoi12@mgh.harvard.edu. Fax: 617-643-2604.

#Author Contributions

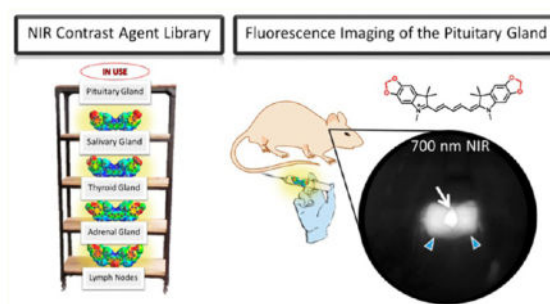
These authors contributed equally.

Notes

The authors declare no competing financial interest.

Supporting Information

The Supporting Information is available free of charge on the ACS Publications website at DOI: 10.1021/acs.jmedchem.6b00038. instrumentation, general methods, synthetic procedures, and NMR and MS spectra (PDF) SMILES information (CSV)



INTRODUCTION

During endocrine surgeries and intricate surgical resections, surgeons mostly rely on their naked eye and experience during often-lengthy procedures to avoid sensitive glands and tissues.¹⁻³ Neglecting to carefully navigate the surgical field can lead to poor patient prognosis even morbidity.⁴⁻¹¹ Endocrine and exocrine tissues regulate the body's hormone levels, and any perturbation, especially transection, can jeopardize the patient's ability to recover after surgery and maintain proper hormone levels.¹²⁻¹⁵ The important task of avoiding sensitive tissues is often difficult as these small and imperative glands are often obscured by blood and surrounding tissues. Surgeons require an imaging modality that can allow them to visualize these tissues during cancer resection surgeries to improve the surgical success rate, lower overall fatalities, and advance patient prognoses.

Near-infrared (NIR) fluorescence-guided resection of cancerous tissues has demonstrated significant promise with increasing advancements being reported over the recent years.¹⁵⁻²⁷ Unfortunately, research efforts have been overwhelmingly concentrated on developing cancer-specific NIR-fluorophores with optimal optical, physicochemical, and targeting properties. This only satisfies one-half of the main objective: the ability to simultaneously image the surgical field with both a disease-targeted fluorophore and a native-tissue-targeted fluorophore of distinct wavelengths that can both be simultaneously and separately detected for direct dual-target imaging in real time.

Significant advancements have been made to develop NIR-fluorescent compounds that target sensitive endogenous tissue and help surgeons avoid these hormonal glands in real time without changing the overall look of the surgical field. The class of NIR-fluorescent cyanine dyes has shown excellent promise in the area of NIR-fluorescence image-guided surgery for in vivo tumor targeting. Cyanine chromophores are broadly defined by having two nitrogen-containing heterocycles that are connected through an electron-deficient polymethine bridge with a delocalized monocation conjugated between both nitrogen atoms. The wavelengths associated with these compounds are heavily dependent on the length of the polymethine bridge and the terminal heterocyclic moieties. Polymethine cyanines are chemically stable NIR-fluorescent compounds, and we have investigated the pentamethine class of compounds previously^{16,20} and herein for laying the groundwork for endogenous tissue targeting. The heptamethine cyanine class (~800 nm fluorescence) has been more extensively explored for disease targeting through the development of zwitterionic decorated heptamethine cyanines

linked with a propionic acid and conjugated with a small cyclic peptide (cRGD-ZW800–1).^{10,21,22} The longer NIR wavelengths (i.e., 800 nm) are more easily detected against the background and usually reserved to detect occult cancerous metastasis due to the minimal autofluorescence. We plan to further exploit the 700 nm channel (pentamethine cyanines) for native tissue imaging for dual channel intraoperative imaging.

Toward achieving this goal, we have continued to harness the structure-inherent tissue affinity to determine the innate biodistribution and targeting by modulating overall molecular characteristics such as hydrophobicity (determined through log *D* calculations), total polar surface area, molecular size/weight, and the electronic contributions (electron-donating/-withdrawing characteristics).^{15,24,26} The compounds synthesized and analyzed herein vary by their heterocyclic moieties (electron donating or withdrawing) and various halogenation at the central carbon atom of the polymethine chain which alters the net dipole, volume, polarization, and even the overall shape of the compounds. We expect these selected modifications to offer biological perturbation toward understanding the molecular characteristics for targeting specific tissues. Correlating these molecular descriptors with in vivo biodistribution is expected to result in a clinically significant paradigm in the quest of translating NIR-targeted contrast agents into the clinic, and every analyzed compound offers another evidentiary piece to the puzzle.

RESULTS AND DISCUSSION

Synthesis of Pentamethine Fluorophores

Since it has been previously reported that halogenated hydrocarbons localize in higher concentration within endocrine and exocrine glands compared to their nonhalogenated counterparts,¹⁶ we decided to probe the effect of halogenation on pentamethine cyanines for endocrine and exocrine tissue targeting. For a direct comparison, we synthesized electron-donating counterparts that could offer insight into how potential electronic factors present in the compounds may influence biodistribution. We selected methoxy and methylene-dioxy heterocyclic groups for a direct comparison to the halogenated counterparts and fully expected perturbation in the biological distribution profile, but we could not predict the results of these modifications. Understanding the effects that altering physicochemical properties imparts on the distribution adds important fundamental knowledge about future targeting ability for this and many other classes of imaging agents.

We have developed several optimized synthetic routes for maximizing the structural diversity in the pentamethine cyanine pharmacophore. The compounds with neutral effects and electron-withdrawing groups are synthesized starting with the corresponding phenyl hydrazine salts being refluxed in the presence of 3-methyl-2-butanone in acidic conditions. This reaction furnishes the indolenines **2–5** in excellent yield. We then alkylated the obtained oil using iodomethane in acetonitrile, which yields the cationic salt **6–10** bearing an acidic methylene proton. We also separately react aniline with a warm ethanolic solution of either mucochloric or mucobromic acid to obtain the pentamethine precursor **12** or **13**, with **11** being commercially obtained. These two compounds are individually combined in the presence of acetic anhydride and either triethylamine (fluorine-containing compounds) or

sodium acetate and are heated to afford the brilliant blue pentamethine fluorophores Schemes 1 and 2.

The electron-donating containing methoxy-substituted compounds are prepared through an identical synthetic route; however, the final step requires a longer reaction time at a slightly elevated temperature, due to the methoxy group electron-donating effects which increases the pK_a of the methylene proton resulting in reduced reactivity of the methylene carbon. We also designed a complementary set of compounds bearing heterocyclic-donating groups features the methylene dioxy ring shown in compounds **36–38**. These compounds are prepared using an alternate synthetic strategy beginning with the acidic bromination of 3-methyl-2-butanone followed by S_N1 replacement of the tertiary bromine by the methylene dioxyaniline compound. Upon heating in the presence of acid catalyst, *para*-toluenesulfonic acid, the compound forms the cyclic methylene dioxy 2,3,3-trimethyl-indolenine ring through a largely unexplored Bischler–Möhlau method that can be alkylated using aforementioned conditions for the formation of compound **35**. The final methylene dioxy compounds **36–38** were synthesized using similar chemistry as the methoxy group (Scheme 3).

Optical and Physicochemical Properties

The optical properties, shown in Table 1, were performed in several solvents to determine the in vivo success for the fluorophores. We can see that the compounds with hydrogen, chlorine, bromide, and methoxy groups (**14–25**, **31–33**) exhibit sharp and NIR absorbance bands with very high molar absorptivity all being $>100,000 \text{ M}^{-1} \text{ cm}^{-1}$ which suggests that these fluorophores will satisfactorily absorb NIR wavelengths in vivo and will be compatible with the intraoperative imaging system. As expected, the methylenedioxy compounds exhibited slightly lower molar absorptivity due to a broadening of the absorption profile which results from a more widely dispersed energy sublevels. Similarly, the trifluoromethyl substituted compounds are very poor at absorbing light at their wavelength of maximum absorbance, as indicated by their low molar absorptivity values in Table 1. We attribute this to the high-electron-withdrawing characteristics of the trifluoromethyl groups which lowers the overall probability of electron movement across the methine bridge connecting the aza-heterocycles. The in vivo success of these compounds also depends of the quantum yield and more importantly the molecular brightness (determined as the product of extinction coefficient and quantum yield) of the compounds in serum; therefore, we examined the quantum yield of these fluorophores in fetal bovine serum (FBS). Compounds **14–28**, **31–33** exhibit high quantum yield values in serum which is very appealing. All of the synthesized compounds have sufficiently high molecular brightness values in serum, with many compounds exhibiting molecular brightness values of $>20,000$. We observed an overall trend for the majority of compounds that as the size of the central halogen increases, the molecular brightness decreases. When analyzing the minimized three-dimensional structures, we see that the *meso*-halogenation perturbs the *trans*-pseudoalkene angles and the elongated structure of the fluorophore which actually shortens the overall length and perturbs the conjugated bridge by requiring the compound to bend to accommodate this central substitution. This is an interesting finding since upon first glance, it seems that adding larger groups to the middle of the compound would result in an elongation of the compound simply

because it would force the neighboring hydrogen atoms apart. Another potential explanation for the decrease in molecular brightness is the heavy atom effect that can effectively stabilize the triplet state, allowing for a higher probability for competing decay processes of the excited state (i.e., phosphorescence or energy transfer) compared to the nonhalogenated fluorophores.

Photostability studies were performed on a select number of contrast agents to observe their performance when continuously irradiated and can be seen in Figure 1. The selected compounds featuring a hydrogen atom at the *meso* position of the polymethine bridge showed little decomposition after being exposed to light for 48 h, however, when chlorine or bromine replace the hydrogen, there is noticeable degradation of up to 35% of the original absorbance. Only a minimal 4% absorbance was lost for each of the first compounds in each set; furthermore, these data help conclude that these compounds would be applicable for long-duration surgical resections with the ability to absorb and fluoresce NIR-light for high-contrast imaging with a half-life of >48h for the entire set studied. The studies were compared to the same concentration of dyes kept in dark containers, but the same distance from the lamp to determine if thermal degradation contributed as well. We found an absence in measurable degradation for the samples kept in the dark which leads us to conclude that heat from the lamp imparts a negligible effect and the absorbance decrease comes from irradiation.

Structure-Inherent Targeting Ability of NIR Fluorophores

As native tissue targeting remains predominantly understudied, we focused our attention to the salivary, thyroid, pituitary, adrenal glands, lymph nodes, and pancreas. As these tissues facilitate the regulation of human hormone levels, they are important for long-term health and should be carefully avoided during surgical resection in surrounding areas.

After *in vivo* studies, we found compounds that exhibited high SBR in targeted tissues (high is designated as a ratio of target signal to surrounding tissue being >2.0). Without surface or subcellular receptors readily available for the particular native tissues, it has been difficult to infer mechanistic insight of how these fluorophores localize within their respective tissues. However, we have found several key structural components that help facilitate structure-inherent biodistribution and localization in important tissues, including the salivary, thyroid, pituitary, adrenal glands, lymph nodes, and pancreas.

In surgical resections such as thyroidectomies, it is crucial to remove the entire thyroid gland while maintaining complete integrity of the parathyroid gland. Selective thyroid gland imaging is paramount in the ability to avoid partial thyroid resection or accidental parathyroid transection which can cause several abnormal human conditions such as hypocalcemia.

The common clinical indications of salivary gland imaging are pain and swelling. Imaging is useful in identifying the masses of salivary glands and also in differentiating them from the masses/pathologies of adjacent cervical spaces. In proven cases of salivary gland tumors, imaging helps in delineating the extent of the lesion and invasion of adjacent cervical spaces.

Cancerous tissues in this area can grow quickly, and surgical resection of the diseased tissue is needed while sparing excision of the exocrine salivary glands themselves.

Toward finding the thyroid and salivary glands targeting by using NIR fluorophores, we evaluated the imaging capability of these compounds in thyroid and salivary glands. Table 3 shows the thyroid and salivary glands targeting for the entire set of compounds. The targeting of these two tissues seemed to parallel each other, suggesting a biological connection between these two tissues, though despite an extensive literature review, an explanation for this remains unclear. Among the entire set of prepared compounds, we found that central halogenation reduced the targeting efficacy into these glands. Surprisingly, the parent set of compounds (**14–16**) all targeted the salivary gland with superior SBR. From our data, we can see overall that the salivary glands are sensitive to the central halogenation but remain tolerant to the heterocyclic halogen incorporation. Compounds **20–25** exhibit the halogen trend we observed. With the heterocyclic halogen substitution, the salivary gland targeting remains high; however, when the central halogen is incorporated within the same compounds, we have a severely diminished targeted ability (i.e., from compound **20** with SBR of >5 to compounds **21** and **22** with SBR of 1–2). Specifically compounds **17–25** shown in Figures 2 and 3 exemplify this trend. Compounds **17**, **20**, and **23** do not feature halogens at the central carbon of the polymethine chain and exhibit the most effective thyroid and salivary gland localization. As the halogen incorporation increases, the thyroid and salivary gland localization is forfeited in deference to nonspecific accumulation and high liver uptake due to hepatobiliary clearance arising from the increase in hydrophobicity.

As one of the important endocrine glands, the pituitary gland (dubbed the master gland) is responsible for controlling the hormonal release of signaling chemicals throughout the body. Transecting this precious gland during surgery causes lasting side effects from hormone dysregulation with imbalances perpetuating during the lifetime of the patient. Tumors associated with the pituitary gland can interfere with signaling the release of many hormones such as thyroid-stimulating hormone which directly influences metabolic activity, energy levels, growth hormones, and the nervous system. Efforts to remove pituitary gland tumors must critically and clearly image the native tissue to prevent accidental damage. We found excellent pituitary gland targeting with the trifluoromethyl compounds **26–28** (Figure 4). The trifluoromethyl substitutions increase the dipole of the compound considerably (Table 2) which we anticipated to elicit a drastic biological response compared to the alternate halogenated counterparts. Indeed, the vast change in electronic dipole from 1 to 4 debye (other compounds) to >7.5 debye in the trifluoromethyl substituted compounds (which also corresponds to an increase in polarizability) lowered the target recognition to some endocrine tissues; however, the thyroid gland targeting remained elevated when the central position was halogen-free.

Lymph nodes are widely distributed and are responsible for immune system function and can indicate an abnormal physiological condition. For example, an increase in size may indicate leukemia due to increased trafficking of lymphocytes from the blood into the lymph nodes. Additionally, thorough examination of the lymph nodes is crucial for the staging of cancer as tumor metastases normally first localize in sentinel lymph nodes. For surgical avoidance and the frequent necessity to biopsy, a NIR imaging technique to visualize this

tissue is highly important. In the developed set of compounds, we noticed effective targeting of the lymph node by the methoxy derivatives **31–33** which is surprising in the context of the methylene dioxy compounds **36–38** exhibiting low lymph node targeting. Interestingly we see an inverse effect of the previous set of compounds where the *meso* halogenation increases the imaging signal as compared to the surrounding tissue in the lymph node with **32** and **33** having a SBR of >5 as indicated by the +++ in Table 3. Figure 5 shows two successful examples of nodal imaging in the inguinal and lumbar nodes with compound **33** exhibiting excellent targeting characteristics.

The adrenal glands, located above the kidney, produce essential and nonessential hormones that primarily control the body's metabolism, blood pressure, and stress response. In Figure 6, we observed that the methylene dioxy compounds **36–38** exhibited adrenal gland targeting characteristics (++, SBR 3–5) that also seemed to be tolerant to the addition of *meso*-halogens. It seems that the log *D* values predominantly govern the localization of these compounds as the five compounds (**31, 32, 36–38**) with the lowest log *D* were the most effective at targeting this tissue, with the methylene dioxy compounds **36–38** prevailing as the best contrast agents for the adrenal gland across the series. This finding is also true in their pancreas targeting ability, as all three compounds within this set exhibit excellent SBR in pancreatic tissue. Interestingly, the small change from methoxy **31–33** to the locked ring structure of **36–38** alters the targeting ability of the compound (i.e., comparing **33** and **38**). This finding also corroborates our previous results that pancreatic targeting requires low comparative log *D* values. Indeed the highest pancreas targeting characteristics are from compounds exhibiting comparatively low log *D* values (i.e., compounds **36–38**, log *D* 2.80–3.21). Additionally, the central halogenation seems to lower pancreas-targeting substantially, except for the methylene dioxy set of compounds. It is very interesting that independent halogenation (either central or terminal heterocycles) does not seem to greatly perturb the pancreatic tissue uptake, except for when the trifluoromethyl group is incorporated. Halogenating both positions, however, has a detrimental effect on the compound-pancreas localization. For example, compounds **15, 16, 17, 20, and 23** are all effective at pancreas targeting, and only have halogens at either the heterocycles or bridge. Compounds **18, 19, 21, 22, 24, and 25** with all sites halogenated exhibit reduced pancreas uptake. We attribute this effect to an increase in overall hydrophobicity imparted by too many halogens on the core structure. Additionally, structures with higher molecular weight in addition to greater hydrophobic character seem to be poor at pancreatic localization.

Preliminary Cytotoxicity of NIR fluorophores

To confirm cell cytotoxicity of the tissue-specific fluorophores, NIH/3T3 mouse fibroblast cells were incubated with the selected NIR fluorophores, respectively, for 1 h at 37 °C and gently washed with DMEM. Then, the viability of fibroblasts was assessed by the alamarBlue assay. The assay system incorporates an oxidation–reduction (REDOX) indicator that both fluorescence and changes color in response to chemical reduction of growth medium resulting from cell growth. As shown in Figure 7, over 75% of the cells were viable when treated with NIR fluorophores at concentrations of 2 μM and 10 μM . Therefore, notable cell death was not observed even with the high concentration of the NIR

fluorophores. These results confirm that tissue-specific NIR fluorophores do not show obvious cytotoxic effects.

CONCLUSIONS

Toward satisfying the clinical need for native tissue targeted contrast agents in real-time NIR image-guided surgery, we present compounds that are effective at imaging the salivary, thyroid, pituitary, adrenal glands, lymph nodes, and pancreas. We are confident that this work will lay the foundation for development of native tissue contrast agents for clinical use.

EXPERIMENTAL DETAILS

Synthesis of Pentamethine Cyanine Analogs

The chemical reagents used in the synthesis of these compounds were obtained from Acros Organics, Alfa Aesar, and Matrix Scientific. The reactions were followed using silica gel 60 F₂₅₄ thin-layer chromatography plates (Merck EMD Millipore, Darmstadt, Germany). Open column chromatography was utilized for the purification of all final compounds using 60–200 μm , 60A, classic column silica gel (Dynamic Adsorbents, Norcross, GA). The ¹H NMR and ¹³C NMR spectra were obtained using high-quality Kontes NMR tubes (Kimble Chase, Vineland, NJ) rated to 500 MHz and were recorded on a Bruker Avance (400 MHz) spectrometer using DMSO-*d*₆ or MeOD-*d*₄ containing tetramethylsilane (TMS) as an internal calibration standard set to 0.0 ppm. UV–vis/NIR absorption spectra were recorded on a Varian Cary 50 spectrophotometer. High-resolution accurate mass spectra (HRMS) were obtained either at the Georgia State University Mass Spectrometry Facility using a Waters Q-TOF micro (ESI-Q-TOF) mass spectrometer or utilizing a Waters Micromass LCT TOF ES+ Premier mass spectrometer. Liquid chromatography utilized a Waters 2487 single wavelength absorption detector with wavelengths set between 640 and 700 nm depending on the particular photophysical properties. The column used in LC was a Waters Delta-Pak 5 μM 100A 3.9 \times 150 mm reversed-phase C₁₈ column. Evaporative light-scattering detection analyzes trace impurities that cannot be observed by alternate methods; a SEDEX 75 ELSD was utilized in tandem with liquid chromatography. The integral under the curve was determined for both the LC and ELSD spectra and was used to confirm the purity (>95%) of the synthesized contrast agents.

Optical and Physicochemical Property Analyses

All optical measurements were performed in various solvents, including ethanol, dimethyl sulfoxide (DMSO), phosphate buffered saline (PBS, pH 7.4), and at 37 °C in 100% FBS buffered with 50 mM HEPES, pH 7.4. Absorbance and fluorescence emission spectra of the series of NIR fluorophores were measured using Varian Cary 50 absorbance spectrophotometer (190–1100 nm) and Shimadzu RF-5301PC spectrofluorometer (350–1000 nm). For fluorescence quantum yield (QY) measurements, rhodamine 800 in absolute ethanol (QY = 28%) was used as a calibration standard, under conditions of matched absorbance at 620 nm. In silico calculations of physicochemical distribution coefficient (log *D* at pH 7.4) was calculated using Marvin and JChem calculator plugins (ChemAxon,

Budapest, Hungary). Electrostatic maps were calculated using Spartan DFT calculations at the B3LYP level.

Photostability Analysis

The photostability experiments were performed to determine the photobleaching threshold of the fluorophores. We determined the photobleaching rate by measuring the decrease in absorbance at the wavelength of maximum absorption over a 48h time period. The light condition involved a glass cell containing individual contrast agent (0.01 mm in methanol) that was affixed 250 mm away from a 15W F15T8 broad spectrum bulb being irradiated using a portable lamp at room temperature. The dark control was also examined to exclude chemical decomposition phenomena. The absorbance values were measured at various time points and then plotted versus time to obtain the photostability graphs in light and dark.

Liquid Chromatography–Mass Spectrometry Analysis

The purity of all compounds was measured using liquid chromatography–mass spectrometry (LC-MS) on a Waters system consisting of a 1525 binary HPLC pump with a manual 7725i Rheodyne injector, a 996 photodiode array (PDA) detector, and a 2475 multiwavelength fluorescence detector. The column eluent was divided in 2 using a flow splitter (Upchurch Scientific). A portion of the eluent flowed into an ELSD (Richards Scientific) while the rest flowed into a Micromass LCT ESI-TOF spectrometer (Waters) equipped with a Symmetry (R) C18 (4.6 × 150 mm, 5 μm) reverse-phase HPLC column. For mass spectrometry, the mobile phase was solvent A = 0.1% formic acid in water and solvent B = CH₃CN with 95% A for 5 min and a linear gradient from 5% to 40% CH₃CN (from A to B for 30 min) at a flow rate of 1 mL/min, capillary voltage was –3317 V, and sample cone voltage was –50 V.

Cell Viability Assay

The cell toxicity and proliferation were assessed by alamarBlue (Thermo Scientific) assay. The NIH/3T3 fibroblasts were seeded onto 96-well plates (1 × 10⁴ cells per well). To test cytotoxicity depending on the fluorophore type and concentration, cells were treated with 2 and 10 μM of each NIR fluorophore ($n = 6$) for 1 h and cultured at 24 h post-treatment. At each assay time point, the incubation cell media was replaced with 100 μL of fresh media. Ten μL of alamarBlue solution was directly added to 100 μL each well and incubated for 4 h at 37 °C in a humidified 5% CO₂ incubator. Finally, the 96-well plates were placed into a microplate reader (Spark 10M, TECAN, Switzerland) for measuring the absorption intensity at 570 nm and fluorescence intensity at 590 nm. The data were presented by dividing by dye-untreated control group. The statistical significance was determined by one-way analysis of variance (ANOVA).

Animal Models and Biodistribution

Animals were housed in an AAALAC-certified facility and were studied under the supervision of BIDMC's IACUC in accordance with the approved institutional protocol no. 057-2014. Male CD-1 mice (20–30 g, 6–8 weeks, Charles River Laboratories, Wilmington, MA) were anesthetized with 100 mg/kg ketamine and 10 mg/kg xylazine intraperitoneally (Webster Veterinary, Fort Devens, MA). For intraoperative imaging and biodistribution, the

imaging system equipped with a custom filter set (Chroma Technology Corporation, Brattleboro, VT) composed of a 650 ± 22 nm excitation filter, a 680 nm dichroic mirror, and an 710 ± 25 nm emission filter was used at a fluence rate of 4 mW/cm^2 , with white light (400–650 nm) at 40,000 lx. Color and NIR fluorescence images were acquired simultaneously with custom software at rates up to 15 Hz over a 15 cm diameter field of view. The imaging system was positioned at a distance of 18 in. from the surgical field. For each experiment, camera exposure time and image normalization were held constant.

Quantitative Analysis

At each time point, the fluorescence and background intensity of a region of interest (ROI) over each tissue was quantified using custom imaging software and ImageJ software (NIH, Bethesda, MD) version 1.45q. The signal-to-background ratio (SBR) was calculated as $\text{SBR} = \text{fluorescence}/\text{background}$, where background is the signal intensity of neighboring tissues such as muscle or skin obtained over the period of imaging time. All NIR fluorescence images for a particular fluorophore were normalized identically for all conditions of an experiment. At least three animals were analyzed at each time point. Statistical analysis was carried out using the unpaired Student's *t*-test or one-way ANOVA. Results were presented as mean \pm SD, and curve fitting was performed using Prism version 4.0a software (GraphPad, San Diego, CA).

Synthesis and Characterization of NIR Fluorophore

To obtain the final dyes **14–28**, **31–33**, and **36–38**, the precursor salts **6–10**, **30**, and **35** (2 mol equiv) were added to a clean, dry round-bottom flask. The compounds were stirred in 10 mL of acetic anhydride, and either sodium acetate or triethyl amine (3 mol equiv) was added along with 1 mol equiv of individual malondialdehyde linker **11–13**. The reaction was allowed to stir at 40–60 °C for 2 h. The reactions were monitored closely using regular phase thin-layer chromatography with a mobile phase of DCM/MeOH (99:1) as well as UV–vis–NIR spectrophotometer in quartz cuvettes with methanol as a solvent to visualize the absorption band at ~650 nm against that of the starting materials ~400 nm. Upon completion of the reaction, the mixtures were allowed to cool, and the solvent was evaporated. The residue was extracted using DCM and was washed with DI water (3×70 mL). The resulting organic layer was dried under magnesium sulfate, gravity filtered, and evaporated to afford crystals that were washed with diethyl ether (2×50 mL) and hexanes (50 mL) to yield crystals that were dried under vacuum overnight. The pure product was obtained after dissolving in methanol and precipitating with ether several times, or the compounds were isolated using flash column chromatography and 5% methanol in DCM as the eluting solvent. After purification, the compounds were obtained in the designated yields and were fully characterized.

1,3,3-Trimethyl-2-((1E,3E,5E)-5-(1,3,3-trimethylindolin-2-ylidene)-penta-1,3-dien-1-yl)-3H-indol-1-ium iodide (14)—Yield 64%, mp > 260 °C; ^1H NMR (400 MHz, MeOD- d_4) δ : 1.71 (s, 12H), 3.63 (s, 6H), 6.28 (d, $J = 16.0$ Hz, 2H), 6.65 (t, $J = 12.0$ Hz, 1H), 7.24 (t, $J = 8.0$ Hz, 2H), 7.29 (d, $J = 8.0$ Hz, 2H), 7.39 (t, $J = 8.0$ Hz, 2H), 7.48 (d, $J = 8.0$ Hz, 2H), 8.25 (t, $J = 12.0$ Hz, 2H); ^{13}C NMR (100 MHz, MeOD- d_4) δ 27.90, 31.71,

50.50, 104.44, 111.83, 123.31, 126.20, 129.71, 142.56, 144.29, 155.52, 175.28. TOF HRMS m/z [M]⁺ calcd for [C₂₇H₃₁N₂]⁺ 383.2487, found 383.2474.

2-((1E,3Z,5E)-3-Chloro-5-(1,3,3-trimethylindolin-2-ylidene)penta-1,3-dien-1-yl)-1,3,3-trimethyl-3H-indol-1-ium iodide (15)—Yield 64%, mp 230–232 °C; ¹H NMR (400 MHz, MeOD-*d*₄) δ 1.76 (s, 12H), 3.71 (s, 6H), 6.435 (d, *J* = 12 Hz, 2H), 7.32 (t, *J* = 8 Hz, 2H), 7.39 (d, *J* = 8 Hz, 2H), 7.45 (t, *J* = 8 Hz, 2H), 7.54 (d, *J* = 8 Hz, 2H), 8.345 (d, *J* = 12 Hz, 2H). ¹³C NMR (100 MHz, MeOD-*d*₄) δ 25.03, 29.53, 48.55, 98.93, 110.02, 121.00, 121.86, 124.55, 127.43, 140.42, 141.67, 146.72, 174.28. TOF HRMS m/z [M]⁺ calcd for [C₂₇H₃₀N₂Cl]⁺ 417.2098 found 417.2107.

2-((1E,3E,5E)-3-Bromo-5-(1,3,3-trimethylindolin-2-ylidene)penta-1,3-dien-1-yl)-1,3,3-trimethyl-3H-indol-1-ium iodide (16)—Yield 61%, mp 230–232 °C; ¹H NMR (400 MHz, CDCl₃-*d*₁) δ 1.91 (s, 12H), 3.82 (s, 6H), 6.36 (d, *J* = 8 Hz, 2H), 7.16 (d, *J* = 8.0 Hz, 2H), 7.26–7.31 (m, 4H), 7.39–7.44 (m, 4H), 8.93 (d, *J* = 12 Hz, 2H). ¹³C NMR (100 MHz, DMSO-*d*₆) δ 27.04, 31.98, 49.85, 102.61, 112.19, 115.98, 122.94, 125.97, 128.93, 141.78, 143.02, 149.64, 175.14. TOF HRMS m/z [M]⁺ calcd for [C₂₇H₃₀N₂Br]⁺ 461.1592 found 461.1585.

5-Fluoro-2-((1E,3E,5E)-5-(5-fluoro-1,3,3-trimethylindolin-2-ylidene)penta-1,3-dien-1-yl)-1,3,3-trimethyl-3H-indol-1-ium iodide (17)—Yield 78%, mp > 260 °C; ¹H NMR (400 MHz, DMSO-*d*₆) δ 1.68 (s, 12H), 3.59 (s, 6H), 6.23 (d, *J* = 12.0 Hz, 2H), 6.52 (s, 1H), 7.24 (s, 2H), 7.39 (s, 2H), 7.62 (s, 2H), 8.29 (s, 2H). ¹³C NMR (100 MHz, DMSO-*d*₆) δ: 27.27, 31.85, 49.54, 103.64, 103.76, 110.82, 111.07, 112.43, 112.49, 112.59, 112.66, 115.15, 125.54, 139.55, 143.60, 143.69, 154.27, 154.29, 159.32, 161.72, 173.64. TOF HR-MS ESI m/z [M]⁺ calcd for [C₂₇H₂₉F₂N₂]⁺ 419.2299, found 419.2296.

2-((1E,3E,5E)-3-Chloro-5-(5-fluoro-1,3,3-trimethylindolin-2-ylidene)penta-1,3-dien-1-yl)-5-fluoro-1,3,3-trimethyl-3H-indol-1-ium iodide (18)—Yield 37%, mp > 260 °C; ¹H NMR (400 MHz, DMSO-*d*₆) δ: 1.72 (s, 12H), 3.67 (s, 6H), 6.26 (d, *J* = 14 Hz, 2H), 7.29, 7.31 (t, *J* = 6.8 Hz, 8.8 Hz, 2H), 7.52–7.54 (m, 2H), 7.70 (d, *J* = 6 Hz, 2H), 8.41 (d, *J* = 14 Hz, 2H). ¹⁹F NMR (375 MHz, DMSO-*d*₆) δ: -116.67 (s, 2F). TOF HR-MS ESI m/z [M]⁺ calcd for [C₂₇H₂₉F₂ClN₂]⁺ 453.1909 found 453.1914.

2-((1E,3E,5E)-3-Bromo-5-(5-fluoro-1,3,3-trimethylindolin-2-ylidene)penta-1,3-dien-1-yl)-5-fluoro-1,3,3-trimethyl-3H-indol-1-ium iodide (19)—Yield 52%, ¹H NMR (400 MHz, DMSO-*d*₆) δ: 1.72 (s, 12H), 3.67 (s, 6H), 6.26 (d, *J* = 13.2 Hz, 2H), 7.32 (t, *J* = 8.8 Hz, 2H), 7.55–7.52 (m, 2H), 7.70 (d, *J* = 7.6, 2H), 8.46 (d, *J* = 13.6, 2H). ¹⁹F NMR (375 MHz, DMSO-*d*₆) δ: -116.67 (s, 2F). TOF HR-MS ESI m/z [M]⁺ calcd [C₂₇H₂₉F₂N₂Br]⁺ was 497.1404 found 497.1394.

5-Chloro-2-((1E,3E,5E)-5-(5-chloro-1,3,3-trimethylindolin-2-ylidene)penta-1,3-dien-1-yl)-1,3,3-trimethyl-3H-indol-1-ium iodide (20)—Yield 59%, mp > 260 °C; ¹H NMR (400 MHz, DMSO-*d*₆) δ: 1.69 (s, 12H), 3.59 (s, 6H), 6.27 (d, *J* = 14 Hz, 2H), 6.551 (t, *J* = 12.4, 12.0 Hz, 1H), 7.39 (d, *J* = 8.8 Hz, 2H), 7.46 (d, *J* = 8.4 Hz, 2H), 7.80 (s, 2H), 8.32 (t, *J* = 13.2 Hz, 2H). ¹³C NMR (100 MHz, DMSO-*d*₆) δ: 27.30, 31.84, 49.51, 104.09,

112.87, 123.29, 126.16, 128.67, 129.50, 142.23, 143.54, 154.72, 173.65. TOF HR-MS ESI m/z [M]⁺ calcd for [C₂₇H₂₉Cl₂N₂]⁺ 451.1708, found 451.1722.

5-Chloro-2-((1E,3E,5E)-3-chloro-5-(5-chloro-1,3,3-trimethylindolin-2-ylidene)penta-1,3-dien-1-yl)-1,3,3-trimethyl-3H-indol-1-ium (21)—Yield 53%, mp > 260 °C; ¹H NMR(400 MHz, DMSO-*d*₆) δ: 1.72 (s, 12H), 3.67 (s, 6H), 6.26 (d, *J* = 14 Hz, 2H), 7.52 (m, 4H), 7.89 (s, 2H), 8.43 (d, *J* = 13.6, 2H). ¹³C NMR (100 MHz, DMSO-*d*₆) δ: 26.81, 32.15, 49.98, 100.72, 113.62, 123.06, 123.49, 128.80, 130.31, 142.02, 143.83, 147.96, 174.97. TOF HR-MS ESI m/z [M]⁺ calcd for [C₂₇H₂₉Cl₃N₂]⁺ 485.1318 found 485.1317.

2-((1E,3E,5E)-3-Bromo-5-(5-chloro-1,3,3-trimethylindolin-2-ylidene)penta-1,3-dien-1-yl)-5-chloro-1,3,3-trimethyl-3H-indol-1-ium iodide (22)—Yield 69%, mp 252–254 °C ¹H NMR(400 MHz, DMSO-*d*₆) δ: 1.73 (s, 12H), 3.67 (s, 6H), 6.28 (d, *J* = 13.2 Hz, 2H), 7.52 (m, 4H), 7.89 (s, 2H), 8.47 (d, *J* = 13.2 Hz, 2H). ¹³C NMR (100 MHz, DMSO-*d*₆) δ: 26.79, 32.16, 50.03, 102.96, 113.65, 116.40, 123.51, 128.82, 130.35, 141.99, 143.83, 149.98, 175.15. TOF HR-MS ESI m/z [M]⁺ calcd [C₂₇H₂₈BrN₂Cl₂]⁺ was 529.0813 found 529.0810.

5-Bromo-2-((1E,3E,5E)-5-(5-bromo-1,3,3-trimethylindolin-2-ylidene)penta-1,3-dien-1-yl)-1,3,3-trimethyl-3H-indol-1-ium iodide (23)—Yield 62%, mp > 260 °C; ¹H NMR(400 MHz, DMSO-*d*₆) δ: 1.69 (s, 12H), 3.58 (s, 6H), 6.27 (d, *J* = 14 Hz, 2H), 6.56 (t, *J* = 12.4, 12 Hz, 1H), 7.35 (d, *J* = 8.4 Hz, 2H), 7.59 (d, *J* = 8.4, 2H), 7.93 (s, 2H), 8.33 (t, *J* = 13.2 Hz, 2H). ¹³C NMR (100 MHz, DMSO-*d*₆) δ 27.25, 31.71, 49.48, 104.07, 113.33, 117.45, 126.09, 131.51, 142.63, 143.85, 154.86, 173.45. TOF HR-MS ESI m/z [M]⁺ calcd for [C₂₇H₂₉Br₂N₂]⁺ 539.0697, found 539.0695.

5-Bromo-2-((1E,3E,5E)-5-(5-bromo-1,3,3-trimethylindolin-2-ylidene)-3-chloropenta-1,3-dien-1-yl)-1,3,3-trimethyl-3H-indol-1-ium (24)—Yield 72%, mp > 260 °C; ¹H NMR(400 MHz, DMSO-*d*₆) δ: 1.72 (s, 12H), 3.67 (s, 6H), 6.28 (d, *J* = 12.0 Hz, 2H), 7.47 (d, *J* = 8.0 Hz, 2H), 7.63 (d, *J* = 8.0 Hz, 2H), 8.01 (s, 2H), 8.43 (d, *J* = 12.0 Hz, 2H). ¹³C NMR (100 MHz, DMSO-*d*₆) δ: 26.81, 32.17, 49.96, 100.69, 114.05, 118.37, 123.13, 126.26, 131.63, 142.40, 144.11, 147.96, 174.78. TOF HR-MS ESI m/z [M]⁺ calcd for [C₂₇H₂₈Br₂N₂Cl]⁺ 573.0308, found 573.0316.

5-Bromo-2-((1E,3E,5E)-3-bromo-5-(5-bromo-1,3,3-trimethylindolin-2-ylidene)penta-1,3-dien-1-yl)-1,3,3-trimethyl-3H-indol-1-ium iodide (25)—Yield 46%, mp 231–232 °C; ¹H NMR(400 MHz, DMSO-*d*₆) δ: 1.72 (s, 12H), 3.66 (s, 6H), 6.28 (d, *J* = 13.2 Hz, 2H), 7.47 (d, *J* = 8.0 Hz, 2H), 6.64 (d, *J* = 8.4 Hz, 2H), 8.01 (s, 2H), 8.48 (d, *J* = 13.6 Hz, 2H). ¹³C NMR (100 MHz, DMSO-*d*₆) δ: 26.79, 32.11, 50.03, 102.97, 114.07, 116.47, 118.42, 126.27, 131.65, 142.40, 144.13, 150.03, 175.01. TOF HR-MS ESI m/z [M]⁺ calcd [C₂₇H₂₈Br₃N₂]⁺ was 616.9803, found 616.9814.

1,3,3-Trimethyl-5-(trifluoromethyl)-2-((1E,3E)-5-((E)-1,3,3-trimethyl-5-(trifluoromethyl)indolin-2-ylidene)penta-1,3-dien-1-yl)-3H-indol-1-ium iodide (26)—Yield 55%, mp 218–221 °C; ¹H NMR (400 MHz, CDCl₃): δ 1.81 (s, 12H), 3.79 (s,

6H), 6.53 (d, $J = 13.6$ Hz, 2H), 7.11 (t, $J = 13.6$ Hz, 1H), 7.21(d, $J = 8.4$ Hz, 2H), 7.60 (s, 2H), 7.70 (d, $J = 7.6$ Hz, 2H), 8.02 (t, $J = 13.6$, 2H). ^{19}F NMR: (375 MHz, DMSO- d_6): δ 62.00. TOF HRMS m/z $[\text{M}]^+$ calcd for $[\text{C}_{29}\text{H}_{29}\text{N}_2\text{F}_6]^+$ 519.2297, found 519.2393.

2-((1E,3Z)-3-Chloro-5-((E)-1,3,3-trimethyl-5-(trifluoromethyl)-indolin-2-ylidene)penta-1,3-dien-1-yl)-1,3,3-trimethyl-5-(trifluoro-methyl)-3H-indol-1-ium iodide (27)—Yield 71%, mp 226–228 °C; ^1H NMR (400 MHz, CDCl_3): δ 1.91 (s, 12H), 3.87 (s, 6H), 6.47 (d, $J = 13.6$ Hz, 2H), 7.30 (s, 2H), 7.65 (m, 4H), 8.90 (d, $J = 10.4$ Hz, 2H). ^{19}F NMR (375 MHz, DMSO- d_6): δ 62.05. TOF HRMS m/z $[\text{M}]^+$ calcd for $[\text{C}_{29}\text{H}_{28}\text{N}_2\text{F}_6\text{Cl}]^+$ 553.1840, found 553.1996.

2-((1E,3Z)-3-Bromo-5-((E)-1,3,3-trimethyl-5-(trifluoromethyl)-indolin-2-ylidene)penta-1,3-dien-1-yl)-1,3,3-trimethyl-5-(trifluoro-methyl)-3H-indol-1-ium iodide (28)—Yield 71%, mp 226–228 °C; ^1H NMR (400 MHz, CDCl_3): δ 1.91 (s, 12H), 3.87 (s, 6H), 6.46 (bs, 2H), 7.30 (s, 2H), 7.69 (m, 4H), 8.91 (d, $J = 7.2$ Hz, 2H). ^{19}F NMR (375 MHz, DMSO- d_6): δ 62.01. TOF HRMS m/z $[\text{M}]^+$ calcd for $[\text{C}_{29}\text{H}_{28}\text{N}_2\text{F}_6\text{Br}]^+$ 597.1335, found 597.1597.

5-Methoxy-2,3,3-trimethyl-3H-indole (29)—Yield 78%, reddish brown oil; ^1H NMR (400 MHz, DMSO- d_6) δ 1.17 (s, 6H), 2.16 (s, 3H), 3.68 (s, 3H), 6.74 (m, 2H), 7.38 (s, 1H).

5-Methoxy-1,2,3,3-tetramethyl-3H-indol-1-ium iodide (30)— ^1H NMR (400 MHz, DMSO- d_6) δ 1.51 (s, 6H), 2.71 (s, 3H), 3.86 (s, 3H), 3.94 (s, 3H), 7.14 (d, $J = 8.0$ Hz, 1H), 7.47 (s, 1H), 7.81 (d, $J = 8.0$ Hz, 1H).

5-Methoxy-2-((1E,3E,5E)-5-(5-methoxy-1,3,3-trimethylindolin-2-ylidene)penta-1,3-dien-1-yl)-1,3,3-trimethyl-3H-indol-1-ium iodide (31)—Yield 75%, mp 228–230 °C; ^1H NMR (400 MHz, DMSO- d_6): δ 1.66 (s, 12H), 3.56 (s, 3H), 3.81 (s, 6H), 6.17 (d, $J = 12$ Hz, 2H), 6.46 (t, $J = 12$ Hz, 1H), 6.95 (d, $J = 8$ Hz, 2H), 7.30–7.28 (m, 4H), 8.23 (t, $J = 12$ Hz, 2H). ^{13}C NMR (100 MHz, DMSO- d_6): δ 26.48, 30.62, 48.45, 55.29, 102.06, 108.43, 111.02, 112.84, 123.73, 135.80, 142.15, 151.94, 156.98, 171.55. TOF HRMS m/z $[\text{M}]^+$ calcd for $[\text{C}_{29}\text{H}_{35}\text{N}_2\text{O}_2]^+$ 443.2699, found 443.2692.

2-((1E,3E,5E)-3-Chloro-5-(5-methoxy-1,3,3-trimethylindolin-2-ylidene)penta-1,3-dien-1-yl)-5-methoxy-1,3,3-trimethyl-3H-indol-1-ium iodide (32)—Yield 80%, mp 235–237 °C; ^1H NMR (400 MHz, MeOD- d_4) δ 1.73 (s, 12H), 3.67 (s, 6H), 3.85 (s, 6H), 6.34 (d, $J = 12$ Hz, 2H), 6.99 (d, $J = 8.0$ Hz, 2H), 7.14 (s, 2H), 7.29 (d, $J = 8.0$ Hz, 2H), 8.23 (d, $J = 12$ Hz, 2H). ^{13}C NMR (100 MHz, DMSO- d_6) δ 27.05, 31.96, 49.88, 56.33, 99.74, 109.36, 112.76, 114.07, 121.81, 136.50, 143.49, 146.18, 158.51, 173.76. TOF HRMS m/z $[\text{M}]^+$ calcd for $[\text{C}_{29}\text{H}_{34}\text{N}_2\text{O}_2\text{Cl}]^+$ 477.2309; found 477.2327.

2-((1E,3E,5E)-3-Bromo-5-(5-methoxy-1,3,3-trimethylindolin-2-ylidene)penta-1,3-dien-1-yl)-5-methoxy-1,3,3-trimethyl-3H-indol-1-ium iodide (33)—Yield 55%, mp 214–216 °C; ^1H NMR (400 MHz, DMSO- d_6): δ 1.69 (s, 12H), 3.63 (s, 6H), 3.81 (s, 6H), 6.18 (d, $J = 12$ Hz, 2H), 6.97 (d, $J = 8.0$ Hz, 2H), 7.35 (s, 2H), 7.40 (d, $J = 8$ Hz, 2H), 8.38 (d, $J = 12$ Hz, 2H). ^{13}C NMR (100 MHz, DMSO- d_6): δ 26.20, 31.16, 49.13, 55.53, 101.20,

108.56, 112.00, 113.28, 114.41, 135.67, 142.68, 147.32, 157.72, 173.09. TOF HRMS m/z [M]⁺ calcd for [C₂₉H₃₄N₂O₂Br]⁺ 521.1804 found 521.1801.

5,7,7-Trimethyl-6-((1E,3E,5Z)-5-(5,7,7-trimethyl-5H-[1,3]dioxolo[4,5-f]indol-6(7H)-ylidene)penta-1,3-dien-1-yl)-7H-[1,3]dioxolo[4,5-f]indol-5-ium iodide (36)—Yield 38%, ¹H NMR (400 MHz, DMSO-*d*₆) δ : 1.63 (s, 12H), 3.54 (s, 6H), 6.06 (s, 4H), 6.18 (d, *J* = 16.0 Hz, 2H), 6.46 (t, *J* = 16.0 Hz, 1H), 7.13 (s, 2H), 7.28 (s, 2H), 8.16 (t, *J* = 15 Hz, 2H). ¹³C NMR (100 MHz, DMSO-*d*₆) δ : 27.59, 31.89, 49.29, 94.35, 102.18, 103.40, 104.03, 125.11, 134.93, 137.52, 145.55, 148.02, 152.68, 173.32. TOF HRMS m/z [M]⁺ calcd for [C₂₉H₃₁O₄N₂]⁺ 471.2278 found 471.2268.

6-((1E,3E,5E)-3-Chloro-5-(5,7,7-trimethyl-5,7-dihydro-6H-[1,3]-dioxolo[4,5-f]indol-6-ylidene)penta-1,3-dien-1-yl)-5,7,7-trimethyl-7H-[1,3]dioxolo[4,5-f]indol-5-ium (37)—Yield 39%, ¹H NMR (400 MHz, DMSO-*d*₆) δ : 1.66 (s, 12H), 3.63 (s, 6H), 6.10 (s, 4H), 6.21 (d, *J* = 13.6 Hz, 2H), 7.29 (s, 2H), 7.38 (s, 2H), 8.30 (d, *J* = 13.6 Hz, 2H). ¹³C NMR (100 MHz, DMSO-*d*₆) δ : 27.10, 32.20, 49.70, 94.92, 100.10, 102.34, 104.12, 135.49, 137.25, 146.04, 146.12, 148.10, 174.41. TOF HRMS m/z [M]⁺ calcd for [C₂₉H₃₀N₂O₄Cl]⁺ 505.1894 found 505.1871.

6-((1E,3E,5E)-3-Bromo-5-(5,7,7-trimethyl-5,7-dihydro-6H-[1,3]-dioxolo[4,5-f]indol-6-ylidene)penta-1,3-dien-1-yl)-5,7,7-trimethyl-7H-[1,3]dioxolo[4,5-f]indol-5-ium (38)—Yield 27%, ¹H NMR (400 MHz, DMSO-*d*₆) δ : 1.66 (s, 12H), 3.62 (s, 6H), 6.10 (s, 4H), 6.21 (d, *J* = 13.6 Hz, 2H), 7.29 (s, 2H), 7.39 (s, 2H), 8.36 (d, *J* = 13.6 Hz, 2H). ¹³C NMR (100 MHz, DMSO-*d*₆) δ : 27.08, 32.20, 49.76, 94.94, 102.34, 104.14, 113.95, 135.50, 137.22, 146.16, 146.16, 148.02, 174.59. TOF HRMS m/z [M]⁺ calcd for [C₂₉H₃₀N₂O₄Br]⁺ 549.1389 found 549.1368.

Supplementary Material

Refer to Web version on PubMed Central for supplementary material.

Acknowledgments

This study was supported by a Georgia State University dissertation grant to E.A.O. M.H. wishes to thank the Brains and Behavior Grant, the Health Innovation Grant and the Georgia Research Alliance Grant for their financial support. H.S.C. thanks the NIH/NIBIB grant #R01-EB-011523 for their support. E.A.O. was supported through a predoctoral fellowship from the Center for Diagnostics and Therapeutics (CDT). H.H. was financially supported by Chonnam National University (2015). Thank you Andrew Levitz and Nicholas Bruschi for helping with the synthesis.

ABBREVIATIONS USED

NIR	near-infrared
log <i>D</i>	distribution coefficient
SBR	signal-to-noise ratio
DMEM	Dulbecco's modified eagle's medium

ANOVA analysis of variance

References

1. Yokoyama J, Fujimaki M, Ohba S, Anzai T, Yoshii R, Ito S, Kojima M, Ikeda K. A feasibility study of NIR fluorescent image-guided surgery in head and neck cancer based on the assessment of optimum surgical time as revealed through dynamic imaging. *OncoTargets Ther.* 2013; 6:325–330.
2. Ris F, Hompes R, Cunningham C, Lindsey I, Guy R, Jones O, George B, Cahill RA, Mortensen NJ. Near-infrared (NIR) perfusion angiography in minimally invasive colorectal surgery. *Surg Endosc.* 2014; 28:2221–2226. [PubMed: 24566744]
3. Li C, Cao L, Zhang Y, Yi P, Wang M, Tan B, Deng Z, Wu D, Wang Q. Preoperative detection and intraoperative visualization of brain tumors for more precise surgery: a new dual-modality MRI and NIR nanoprobe. *Small.* 2015; 11:4517–4525. [PubMed: 26058947]
4. Zhu N, Huang CY, Mondal S, Gao S, Huang C, Gruev V, Achilefu S, Liang R. Compact wearable dual-mode imaging system for real-time fluorescence image-guided surgery. *J Biomed Opt.* 2015; 20:9610.
5. Chan HH, Siewerdsen JH, Vescan A, Daly MJ, Prisman E, Irish JC. 3D rapid prototyping for otolaryngology-head and neck surgery: applications in image-guidance, surgical simulation and patient-specific modeling. *PLoS One.* 2015; 10:e0136370. [PubMed: 26331717]
6. Zheng J, Muhanna N, De Souza R, Wada H, Chan H, Akens MK, Anayama T, Yasufuku K, Serra S, Irish J, Allen C, Jaffray D. A multimodal nano agent for image-guided cancer surgery. *Biomaterials.* 2015; 67:160–168. [PubMed: 26218742]
7. Ramakrishnan VR, Kingdom TT. Does image-guided surgery reduce complications? *Otolaryngol Clin North Am.* 2015; 48:851–859. [PubMed: 26119761]
8. Al-Qudah M. Image-guided sinus surgery in sinonasal pathologies with skull base/orbital erosion. *J Craniofac Surg.* 2015; 26:1606–1608. [PubMed: 26114509]
9. Xi L, Jiang H. Image-guided surgery using multimodality strategy and molecular probes. *Wiley Interdiscip Rev Nanomed Nanobiotechnol.* 2016; 8:46–60. [PubMed: 26053199]
10. Njiojob CN, Owens EA, Narayana L, Hyun H, Choi HS, Henary M. Tailored near-infrared contrast agents for image guided surgery. *J Med Chem.* 2015; 58:2845–2854. [PubMed: 25711712]
11. Hill TK, Abdulahad A, Kelkar SS, Marini FC, Long TE, Provenzale JM, Mohs AM. Indocyanine green-loaded nanoparticles for image-guided tumor surgery. *Bioconjugate Chem.* 2015; 26:294–303.
12. Liang CH, Di WY, Ren JP, Zhou FM, Hu Y, Mao HJ, Han DM. Imaging, clinical and pathological features of salivary gland adenolymphoma. *Eur Rev Med Pharmacol Sci.* 2014; 18:3638–3644. [PubMed: 25535134]
13. Santhanam P, Oakley C. Pet imaging of the adrenal gland-utility and pitfalls. *Endocr Pract.* 2014; 20:375–377. [PubMed: 24449670]
14. Sumi M, Van Cauteren M, Sumi T, Obara M, Ichikawa Y, Nakamura T. Salivary gland tumors: use of intravoxel incoherent motion MR imaging for assessment of diffusion and perfusion for the differentiation of benign from malignant tumors. *Radiology.* 2012; 263:770–777. [PubMed: 22447854]
15. Hyun H, Park MH, Owens EA, Wada H, Henary M, Handgraaf HJ, Vahrmeijer AL, Frangioni JV, Choi HS. Structure-inherent targeting of near-infrared fluorophores for parathyroid and thyroid gland imaging. *Nat Med.* 2015; 21:192–197. [PubMed: 25559343]
16. Owens EA, Hyun H, Tawney JG, Choi HS, Henary M. Correlating molecular character of NIR imaging agents with tissue-specific uptake. *J Med Chem.* 2015; 58:4348–4356. [PubMed: 25923454]
17. Owens EA, Lee S, Choi J, Henary M, Choi HS. NIR fluorescent small molecules for intraoperative imaging. *Wiley Interdiscip Rev Nanomed Nanobiotechnol.* 2015; 7:828–838. [PubMed: 25645081]
18. Wada H, Hyun H, Vargas C, Gravier J, Park G, Gioux S, Frangioni JV, Henary M, Choi HS. Pancreas-targeted NIR fluorophores for dual-channel image-guided abdominal surgery. *Theranostics.* 2015; 5:1–11. [PubMed: 25553094]

19. Salim MM, Owens EA, Gao T, Lee JH, Hyun H, Choi HS, Henary M. Hydroxylated near-infrared BODIPY fluorophores as intracellular pH sensors. *Analyst*. 2014; 139:4862–4873. [PubMed: 25105177]
20. Park MH, Hyun H, Ashitate Y, Wada H, Park G, Lee JH, Njiojob C, Henary M, Frangioni JV, Choi HS. Prototype nerve-specific near-infrared fluorophores. *Theranostics*. 2014; 4:823–833. [PubMed: 24955143]
21. Choi HS, Nasr K, Alyabyev S, Feith D, Lee JH, Kim SH, Ashitate Y, Hyun H, Patonay G, Streckowski L, Henary M, Frangioni JV. Synthesis and in vivo fate of zwitterionic near-infrared fluorophores. *Angew Chem, Int Ed*. 2011; 50:6258–6263.
22. Choi HS, Gibbs SL, Lee JH, Kim SH, Ashitate Y, Liu F, Hyun H, Park G, Xie Y, Bae S, Henary M, Frangioni JV. Targeted zwitterionic near-infrared fluorophores for improved optical imaging. *Nat Biotechnol*. 2013; 31:148–153. [PubMed: 23292608]
23. Ashitate Y, Kim SH, Tanaka E, Henary M, Choi HS, Frangioni JV, Flaumenhaft R. Two-wavelength near-infrared fluorescence for the quantitation of drug antiplatelet effects in large animal model systems. *J Vasc Surg*. 2012; 56:171–180. [PubMed: 22503225]
24. Hyun H, Owens EA, Wada H, Levitz A, Park G, Park MH, Frangioni JV, Henary M, Choi HS. Cartilage-specific near-infrared fluorophores for biomedical imaging. *Angew Chem, Int Ed*. 2015; 54:8648–8652.
25. Wada H, Hyun H, Vargas C, Genega EM, Gravier J, Gioux S, Frangioni JV, Choi HS. Sentinel Lymph Node Mapping of Liver. *Ann Surg Oncol*. 2015; 22:1147–1155.
26. Hyun H, Wada H, Bao K, Gravier J, Yadav Y, Laramie M, Henary M, Frangioni JV, Choi HS. Phosphonated near-infrared fluorophores for biomedical imaging of bone. *Angew Chem, Int Ed*. 2014; 53:10668–10672.
27. Ashitate Y, Hyun H, Kim SH, Lee JH, Henary M, Frangioni JV, Choi HS. Simultaneous mapping of pan and sentinel lymph nodes for real-time image-guided surgery. *Theranostics*. 2014; 4:693–700. [PubMed: 24883119]

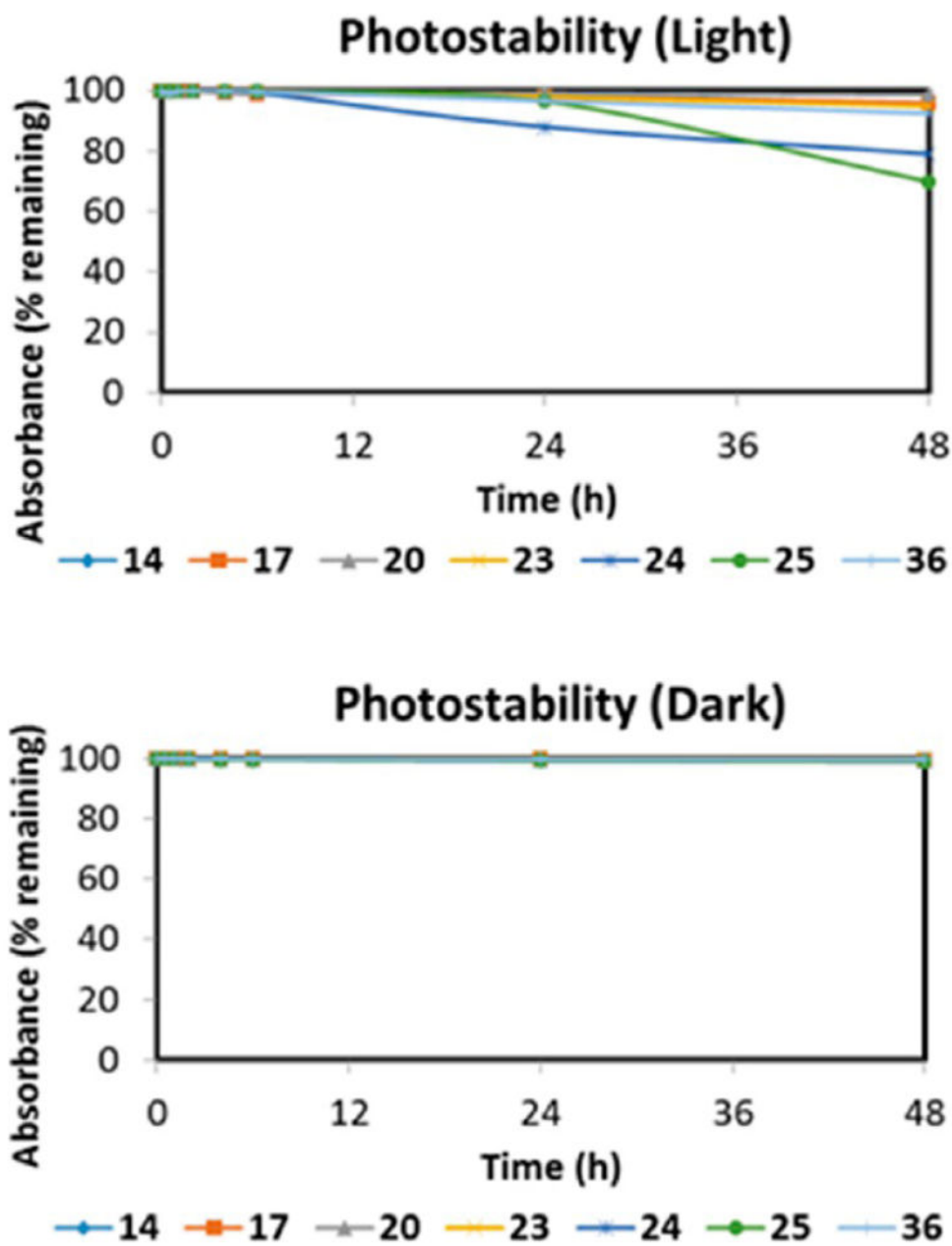
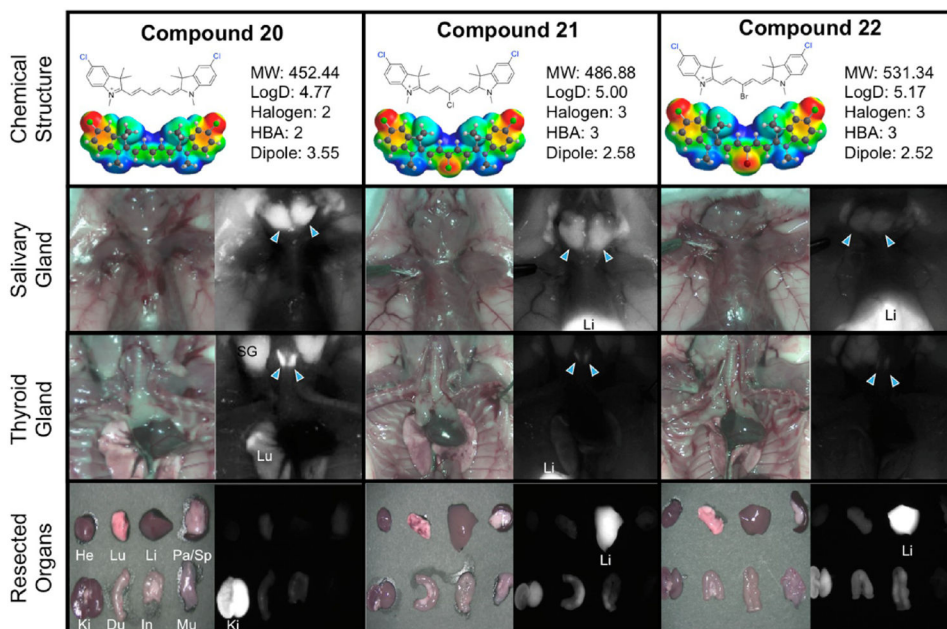


Figure 1. Photodegradation profile in light and dark conditions of a select subset of NIR fluorescent contrast agents. The absorbance values for the individual fluorophores were measured (at the wavelength of maximum absorption) at different intervals to determine the percent absorption remaining.

**Figure 2.**

Compounds **20–22**, targeting to salivary glands and thyroid glands, and biodistribution of resected organs in CD-1 mice. Ten nmol of each fluorophore was injected intravenously into 25 g CD-1 mice 4 h prior to imaging and resection. Abbreviations used are Du, duodenum; He, heart; In, intestine; Ki, kidneys; Li, liver; Lu, lungs; Mu, muscle; Pa, pancreas; SG, salivary gland, Sp, spleen. Arrows indicate the targeted gland.

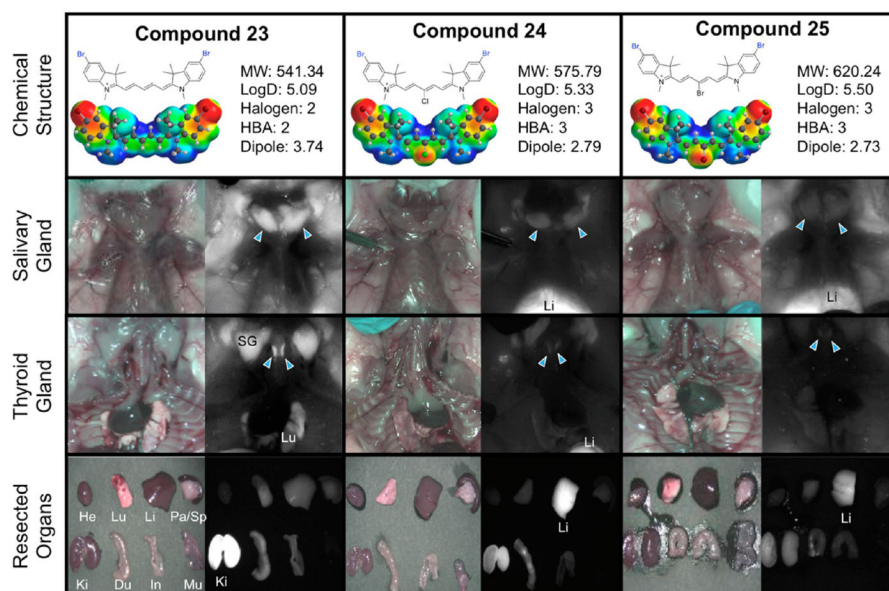


Figure 3. Compounds **23–25**, targeting to salivary glands and thyroid glands, and biodistribution of resected organs in CD-1 mice. Ten nmol of each fluorophore was injected intravenously into 25 g CD-1 mice 4 h prior to imaging and resection. Abbreviations used are Du, duodenum; He, heart; In, intestine; Ki, kidneys; Li, liver; Lu, lungs; Mu, muscle; Pa, pancreas; SG, salivary gland, Sp, spleen. Arrowheads indicate the targeted gland.

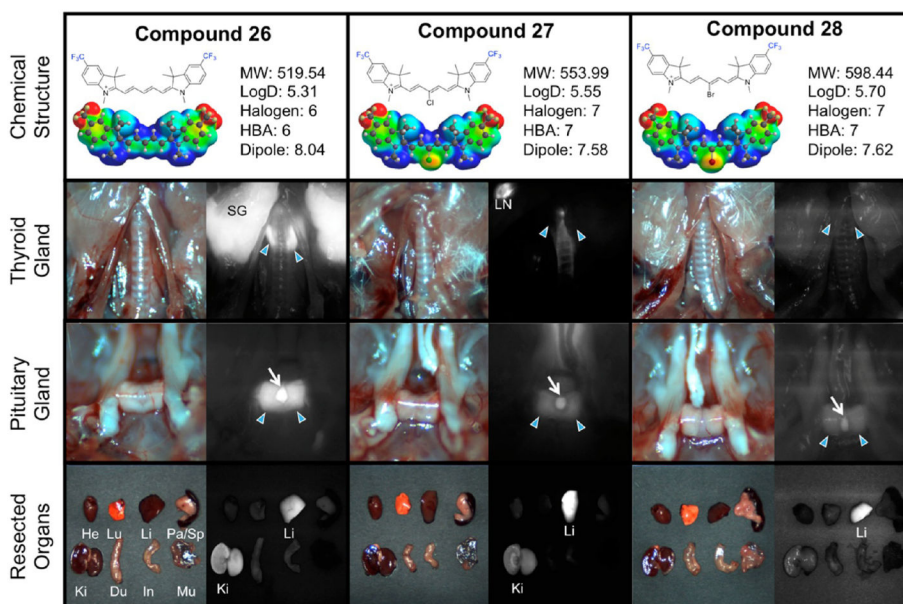


Figure 4.

Compounds **26–28**, targeting to thyroid glands and pituitary gland, and biodistribution of resected organs in CD-1 mice. Ten nmol of each fluorophore was injected intravenously into 25 g CD-1 mice 4 h prior to imaging and resection. Abbreviations used are Du, duodenum; He, heart; In, intestine; Ki, kidneys; Li, liver; LN, lymph node; Lu, lungs; Mu, muscle; Pa, pancreas; SG, salivary gland, Sp, spleen. Arrows indicate the targeted gland. For pituitary glands, arrowheads indicate the anterior portion and arrows for posterior pituitary.

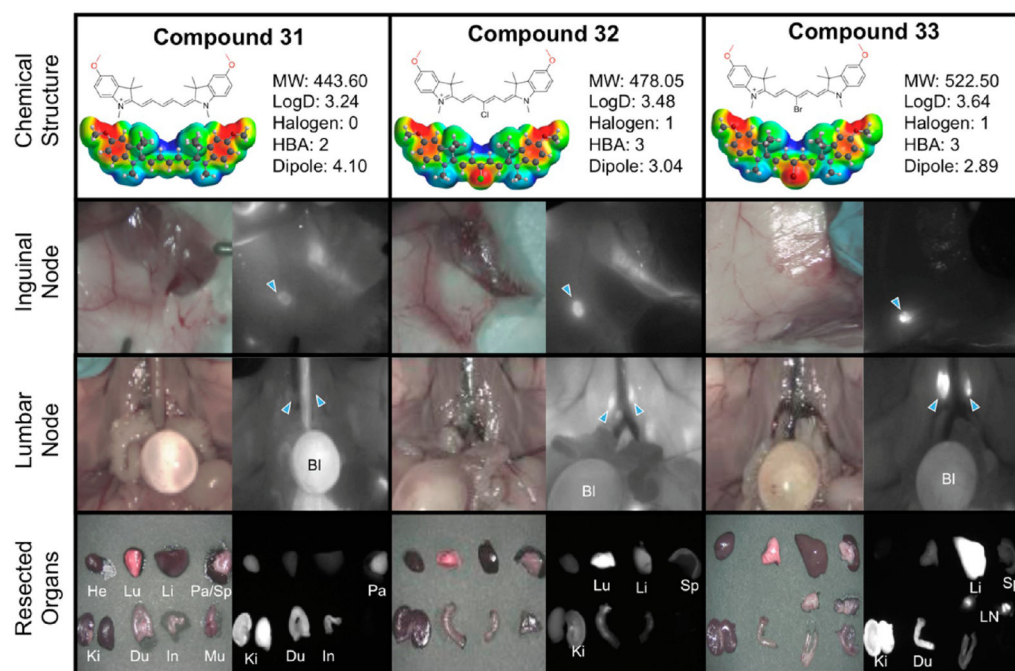
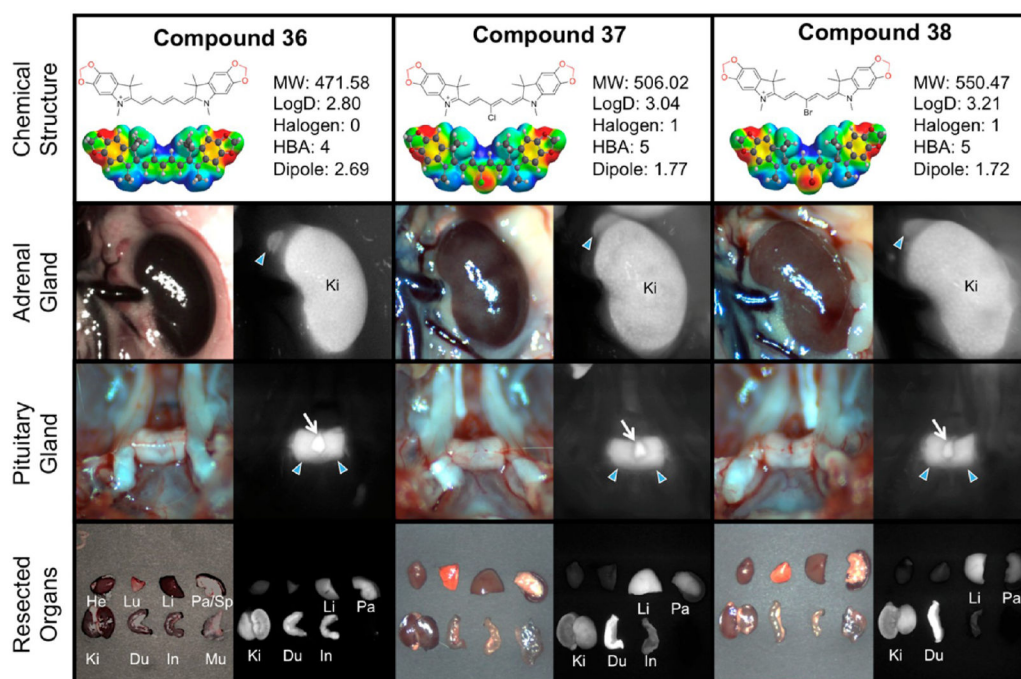


Figure 5. Compounds **31–33**, targeting to inguinal and lumbar lymph nodes, and biodistribution of resected organs in CD-1 mice. Ten nmol of each fluorophore was injected intravenously into 25 g CD-1 mice 4 h prior to imaging and resection. Abbreviations used are Bl, bladder; Du, duodenum; He, heart; In, intestine; Ki, kidneys; Li, liver; LN, lymph node; Lu, lungs; Mu, muscle; Pa, pancreas; Sp, spleen. Arrows indicate the targeted gland.

**Figure 6.**

Compounds **36–38**, targeting to adrenal glands and pituitary gland, and biodistribution of resected organs in CD-1 mice. Ten nmol of each fluorophore was injected intravenously into 25 g CD-1 mice 4 h prior to imaging and resection. Abbreviations used are Du, duodenum; He, heart; In, intestine; Ki, kidneys; Li, liver; Lu, lungs; Mu, muscle; Pa, pancreas; SG, salivary gland, Sp, spleen. Arrows indicate the targeted gland. For pituitary glands, arrowheads indicate the anterior portion and arrows for posterior pituitary.

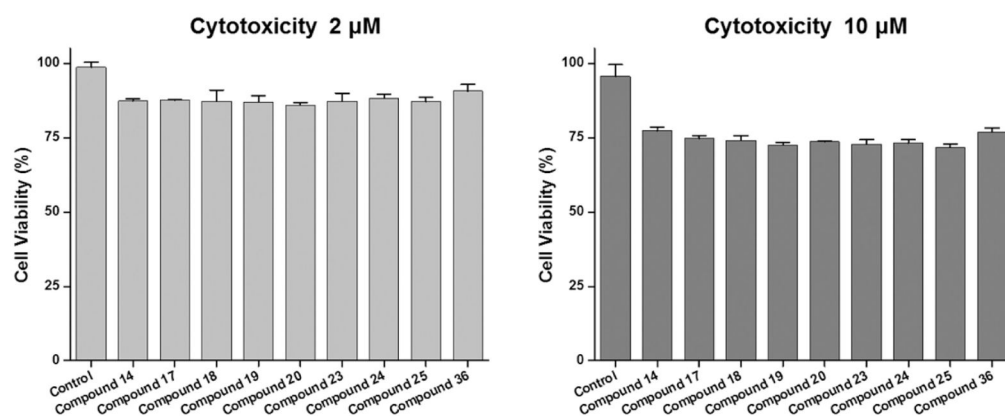
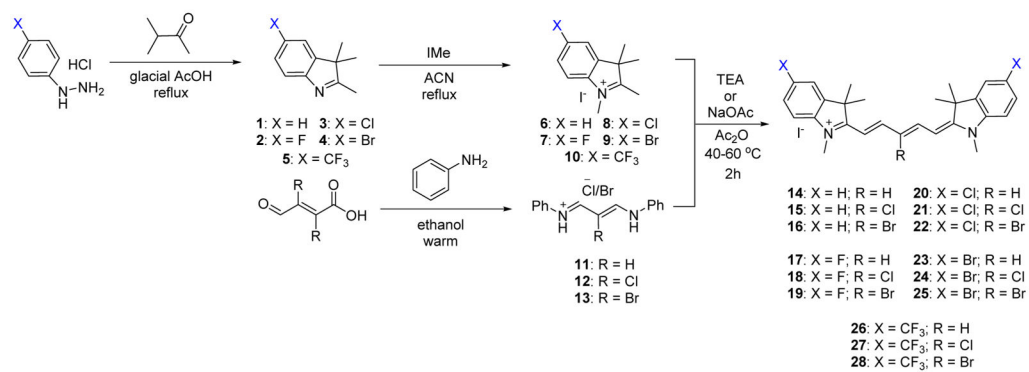
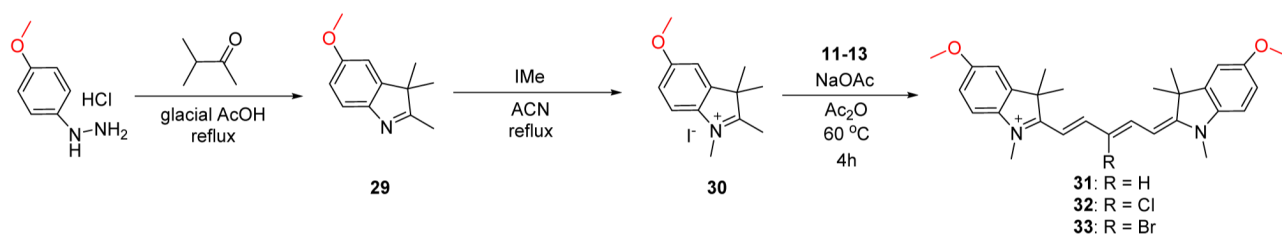


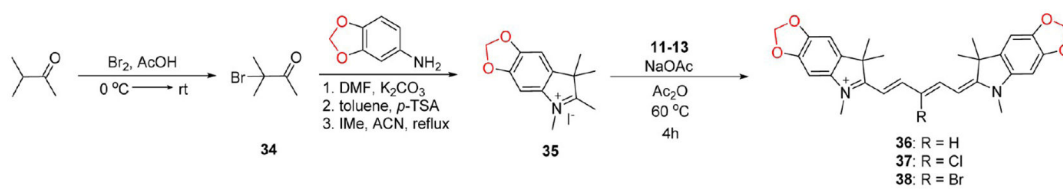
Figure 7. Cell viability assay of selected NIR fluorophores using NIH/3T3 fibroblasts. Cell viability was plotted 1 day post-treatment of compounds at a concentration of 2 μM (left) or 10 μM (right), compared to untreated control as measured by the alamarBlue assay. Data are representative of $N=6$ independent experiments per condition (mean \pm SD).

**Scheme 1.**

Synthesis of 700 nm Emitting Pentamethine Cyanines Featuring Neutral (X = H) and Electron-Withdrawing (X = F, Cl, Br, CF₃) Moieties



Scheme 2.
Synthesis of 700 nm Emitting Pentamethine Cyanines Featuring Electron-Donating Methoxy Groups



Scheme 3.
Synthesis of 700 nm Emitting Pentamethine Cyanines Featuring Electron-Donating Methylene Dioxy Substitution on the Phenyl Rings

Table 1

Optical Properties of 700 nm Emitting NIR Fluorophores^a

ID	λ_{abs} (nm)			extinction coefficient (ϵ , $\text{M}^{-1}\text{cm}^{-1}$)			λ_{em} (nm)			Stokes shift			QY (Φ , %)			MB ($\epsilon \times \Phi$)		
	DMSO	EtOH	PBS	FBS	DMSO	EtOH	PBS	FBS	EtOH	FBS	EtOH	FBS	EtOH	FBS	EtOH	FBS	EtOH	FBS
14	647	645	640	649	212,500	248,200	218,800	184,500	660	662	15	13	32.7	31.0	81,161	57,195		
15	645	644	642	638	235,300	207,800	171,000	168,800	659	665	15	27	29.2	28.8	60,677	48,614		
16	645	641	638	634	257,330	253,200	204,400	211,700	657	660	16	26	30.1	43.6	76,213	92,301		
17	645	641	638	649	216,700	225,800	196,500	164,400	663	662	22	13	31.6	35.2	71,352	58,868		
18	646	643	638	638	210,900	233,700	193,400	193,400	658	660	15	22	16.5	15.3	38,561	29,590		
19	642	641	635	644	173,200	210,500	170,900	145,800	658	658	17	14	16.3	11.9	34,312	17,350		
20	652	649	645	660	183,400	204,200	174,200	136,000	658	669	19	9	41.5	57.5	84,743	78,200		
21	653	652	647	658	192,800	207,800	140,200	136,000	664	666	14	8	18.3	28.5	38,027	38,760		
22	650	648	643	655	233,100	250,600	185,000	153,700	665	663	17	12	15.4	17.4	38,592	26,744		
23	653	650	653	662	181,200	174,500	144,800	141,100	670	671	20	9	42.4	57.0	73,988	80,427		
24	655	653	660	648	140,200	189,600	121,500	119,700	667	671	14	23	20.8	23.0	39,437	27,531		
25	643	641	635	644	169,000	169,600	166,900	159,600	657	663	16	21	15.5	11.8	26,288	18,833		
26	642	638	636	648	41,200	45,200	28,700	30,600	656	654	18	6	58.7	89.2	26,532	27,295		
27	644	640	638	649	72,000	114,900	56,300	19,500	656	655	16	6	20.5	47.4	23,555	9243		
28	641	638	635	644	32,400	49,700	19,600	8400	653	651	15	7	21.1	29.0	10,487	2,436		
31	671	668	658	674	152,300	205,000	133,600	135,000	696	696	28	22	9.6	11.9	19,680	16,070		
32	672	671	658	676	148,100	210,000	135,900	162,000	694	692	23	16	3.9	9.7	8190	15,710		
33	669	669	655	676	94,200	154,000	82,100	109,000	689	688	20	12	5.1	9.7	7218	10,570		
36	691	690	680	698	107,200	108,100	89,200	85,900	705	716	15	18	4.7	6.5	5081	5584		
37	689	690	678	693	147,200	156,600	127,100	117,800	716	712	26	19	3.0	4.2	4698	4948		
38	687	687	675	691	154,900	165,800	135,700	125,000	715	716	28	25	2.9	3.1	4808	3875		

^a All measurements were performed in DMSO, ethanol (EtOH), PBS, and FBS, pH = 7.4 at 37 °C.Abbreviations: λ_{abs} , wavelength of maximum absorbance; λ_{em} , wavelength of maximum emission; QY, quantum yield; and MB, molecular brightness.

Table 2

in Silico Physicochemical Properties of 700 nm Emitting NIR Fluorophores (log *D*, TPSA, and H-bond acceptors) Calculated Using Marvin and JChem Calculator Plugins^a

ID	MW (g/mol)	log <i>D</i> (pH = 7.4)	TPSA	physicochemical properties					polarizability
				H-bond acceptors	length (Å)	volume (Å ³)	dipole (debye)		
14	383.548	3.56	6.25	1	18.665	445.51	1.95	76.14	
15	417.994	3.79	6.25	1	18.530	458.45	0.89	77.21	
16	462.445	3.96	6.25	1	18.453	462.96	0.79	77.55	
17	419.529	3.84	6.25	2	18.684	455.28	4.23	76.95	
18	453.974	4.08	6.25	3	18.536	468.22	3.32	78.02	
19	498.425	4.24	6.25	3	18.475	472.73	3.26	78.36	
20	452.439	4.77	6.25	2	18.674	472.01	3.55	78.30	
21	486.884	5.00	6.25	3	18.539	484.95	2.58	79.37	
22	531.335	5.17	6.25	3	18.464	489.45	2.52	79.71	
23	541.341	5.09	6.25	2	18.665	481.25	3.74	79.05	
24	575.786	5.33	6.25	3	18.517	494.19	2.79	80.12	
25	620.237	5.50	6.25	3	18.340	498.70	2.73	80.40	
26	519.544	5.31	6.25	6	20.188	511.26	8.04	81.47	
27	553.989	5.55	6.25	7	19.547	524.14	7.58	82.54	
28	598.440	5.70	6.25	7	19.406	528.65	7.62	82.88	
31	443.600	3.24	24.71	2	20.631	500.23	4.10	80.61	
32	478.045	3.48	24.71	3	20.527	513.28	3.04	81.68	
33	522.496	3.64	24.71	3	20.142	517.72	2.89	82.02	
36	471.577	2.80	43.17	4	21.203	496.69	2.69	80.33	
37	506.019	3.04	43.17	5	20.847	509.64	1.77	81.39	
38	550.473	3.21	43.17	5	20.680	514.15	1.72	81.74	

^aLog *D* = partition coefficient at pH 7.4, TPSA = total polar surface area, while molecular parameters (length, volume dipole, and polarizability) were calculated using Spartan Wavefunction (V10) DFT starting with the minimized structural conformation of the lowest energy.

Table 3

Targeting Properties and Biodistribution of 700 nm Emitting NIR Fluorophores for Specific Organs/Tissues at 4 h Post-Injection^a

ID	targeted tissues										biodistribution					
	AG	Pa	PG	SG	TG	LN	Li	Ki	He	Lu	Sp	Bo				
14	-	+++	++	+++	++	++	-	+++	+	-	-	++				
15	-	+++	+	+++	+	+	+	+++	-	-	-	+				
16	+	++	-	+++	+	+	+	+++	-	-	-	+				
17	-	+++	++	+++	+++	++	-	+++	-	+	-	+				
18	+	++	+	++	++	++	++	+++	-	+	-	-				
19	-	+	-	+	+	-	++	+++	-	+	-	-				
20	++	+++	+++	+++	+++	+++	-	+++	+	++	-	++				
21	+	+	+	++	+	-	+++	++	-	-	-	-				
22	+	+	-	+	+	-	+++	++	-	+	-	-				
23	+	+++	+++	+++	+++	+++	++	+++	+	++	-	++				
24	+	+	+	++	+	+	+++	++	-	+	-	+				
25	+	+	-	+	+	-	+++	++	-	+	-	-				
26	-	++	+++	++	++	-	+++	++	-	-	-	-				
27	-	+	+	+	-	++	+++	++	-	-	-	-				
28	+	+	-	+	-	-	+++	+	-	-	-	-				
31	++	+++	++	+++	++	++	+	+++	+	+	-	+				
32	++	++	++	++	++	+++	+++	+++	-	-	-	-				
33	+	+	++	++	+	+++	+++	+++	-	+	+	-				
36	++	+++	+++	++	+	+	++	+++	+	+	-	-				
37	++	+++	++	++	++	+	+++	++	-	-	-	-				
38	++	+++	++	++	++	+	+++	++	-	-	-	-				

^a Abbreviations used are AG, adrenal gland; Pa, pancreas; PG, pituitary gland; TG, thyroid gland; SG, salivary gland; Li, liver; Ki, kidneys; He, heart; Lu, lungs; Sp, spleen; Bo, bone; LN, lymph node. The SBR of each organ/tissue relative to the abdominal wall was quantified and labeled as -, 1-2; +, 2-3; ++, 3-5; and +++, >5.